Hindawi
Wireless Communications and Mobile Computing
Volume 2022, Article ID 6387919, 12 pages
https://doi.org/10.1155/2022/6387919

Research Article

Multiobjective Optimization of Structure and Robustness of a Split Parallel Multicomponent Strain Sensor

Peng Kong,[1,2] Xiaoqiang Peng,[1] and Zhenzeng Lian[2]

[1]*Laboratory of Science and Technology on Integrated Logistics Support, National University of Defense Technology, Changsha, 410073 Hunan Province, China*
[2]*China Aerodynamics Research and Development Center, Mianyang, 621000 Sichuan Province, China*

Correspondence should be addressed to Zhenzeng Lian; liansky2020@163.com

Received 29 November 2021; Accepted 26 January 2022; Published 7 March 2022

Academic Editor: Alireza Souri

A novel split parallel multicomponent strain sensor structure layout is proposed based on the special requirements of the helicopter rotor airfoil wind tunnel test for measuring aerodynamic sensors. The sensor consists of two splits with the same configuration; the performance of the sensor not only depends on the split structure of the sensor but also depends on the assembly relationship between the splits. Three steps have been performed so as to enhance the technical performance of the sensor. First, the RBF neural network approximate model and the second-generation nondominated sorting genetic algorithm are used to optimize the split of sensor deterministically; secondly, the rotor airfoil wind tunnel test model and the sensor finite element system model are established, and the 6σ robustness analysis is carried out; finally, the 6σ robust multiobjective optimization has been carried out considering the sensor split processing errors and the assembly errors. The results show that, compared to initial designed sensors, the sensitivity of the three components of the sensor is increased by 285.46%, 284.95%, and 151.5%, respectively, and the maximum equivalent stress is reduced by 28.4%; the interference to the three components is reduced by 97.82%, 92.83%, and 99.8%, respectively, and the quality is reduced by 25.74%. Meanwhile, the quality level of the sensor was promoted, and the sensitivity of the response to assembly and manufacturing errors were reduced. These results exhibit that the structural layout, optimized path, and method in this strain sensor are suitable for the needs of helicopter rotor airfoil wind tunnel test.

1. Introduction

Helicopter rotor dynamic stall is a serious unsteady aerodynamic phenomenon with complex mechanisms, especially the airfoil dynamic stall. Hence, in-depth understanding of the rotor airfoil dynamic stall characteristics is of great importance to investigate the ways to improve rotor performance, predict the rotor aerodynamics more accurately, and thereby promote the development of advanced helicopters.

The wind tunnel test is the main means to understand the dynamic stall characteristics and flow mechanism of the rotor blade airfoil recently. It is necessary to develop a multicomponent strain-type force sensor to support the model through the left and right sides in parallel and accurately measure the model resistance, lift, and pitch moments during the wind tunnel test of the helicopter rotor airfoil.

While in the conventional wind tunnel test, the aircraft model, sensors, and supporting test device are connected in series and connected at a single point, whose precision and accuracy are mainly rely on the performance of the sensor, that is, the sensor's own sensitivity, stiffness, strength, and mutual interference between components [1–4].

Therefore, a novel split parallel multicomponent strain sensor structure layout is proposed consisting of two components, A and B, to meet the needs of the rotor-wing wind tunnel test, on the basis of conventional three-piece beam load cells. A and B are three-component strain sensors with the same configuration, supporting the rotor airfoil wind tunnel test model from both sides in parallel to complete the model aerodynamics and torque measurement. The development of the sensor must consider not only the sensitivity, stiffness, strength, and mutual interference between

the components but also the impact of assembly errors between the A and B components on the overall performance of the sensor.

The following design and optimization approaches are proposed to improve the sensor split and its overall technical performance. Firstly, a finite element analysis model is established with the sensor split as the object to analyze separately its strain under the action of resistance, lift, and pitch moment cloud map and to determine the location of strain gauges and the way of group bridges; secondly, the RBF neural network approximate model and NSGA-II multiobjective optimization algorithm are utilized to deterministically optimize the sensor split performance and obtain the Pareto optimal solution and excellent monomer performance [5]; thirdly, a finite element system model of the rotor airfoil wind tunnel test model and sensor was established. Based on the RSM response surface approximation model and the Monte Carlo simulation technology, the quality level of the system was tested, and the robustness optimization technology was introduced to improve the robustness of the sensor.

2. Materials and Methods

2.1. Geometry. The geometry and main parameters of the sensor splits are shown in Figures 1 and 2. The left and right ends of the split use single-piece beam-type elastic elements (serial number 1) of the same geometric size to bear resistance F_X. The length, width, and height of the single-piece beam-type elastic elements are expressed as L2, B3, and H3; the middle of the split body is a three-beam elastic element; the middle main beam (serial number 2) of the three-beam elastic element bears the lift force F_y; the front and rear side beams (serial number 3) bear the pitching moment M_Z; the length, width, and height of the middle main beam are expressed as L1, B1, and H1; the front and rear side beams have the same geometric dimensions, and their length, width, and height are, respectively, L1, B2, and H2; the thickness of the front and rear flange sensors is S2; and the thickness of the middle flange S1 plays the role of connection.

Each measurement of the elastic element of this layout is independent of the load measurement, that is, it is sensitive to the load of the measured component and insensitive to the load of other components, so it is easy to obtain the required sensitivity and less mutual interference.

2.2. Key Technical Requirements. The split structure of the sensor requires high sensitivity, sufficient strength, rigidity, and small interference between the components.

Sensitivity is an important factor of sensor design which can be improved for the strain-type force sensor by increasing the design strain value of the measuring element. And the design strain value of the general wind tunnel sensor is selected ranging 300~600 $\mu\varepsilon$ [6].

Sufficient strength under the maximum external load is necessary to ensure the safety of the wind tunnel test. The rotor airfoil wind tunnel test's heave motion frequency can reach 5, while the first-order natural frequency of the system composed of strain-type force sensor and rotor airfoil wind tunnel test model must be 10 times than its motion frequency [7].

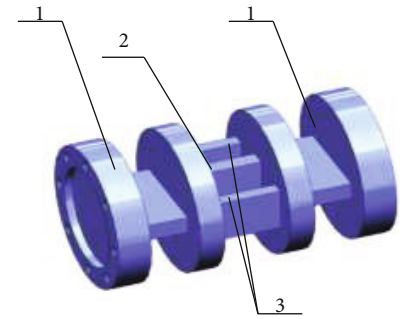

Figure 1: The geometric structure of the sensor split.

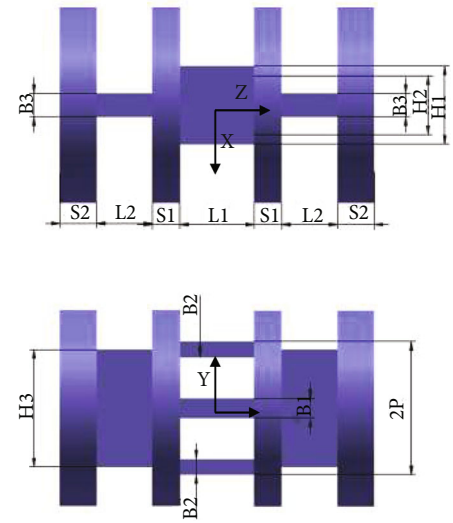

Figure 2: The main geometric parameters of the sensor split.

In the structural design, due to mutual interference between the components, it is necessary to allocate the stiffness reasonably to ensure proper deformation in the load direction of the measured component and reduce its deformation in other components. Generally, the amount of interference between the components of the strain sensor should be controlled below 10% [6].

2.3. Analysis of Split Finite Element Model

2.3.1. Geometry Simplification. The original structure of the model is simplified, especially some local details without affecting the calculation accuracy of the device. These simplifications will not affect the overall analysis results of the original structure but can significantly improve the speed and quality of the finite element analysis and sometimes improve the accuracy and reliability of calculation results.

2.3.2. Meshing. In order to ensure the accuracy of the calculation results, second-order grid elements are used. In order to reasonably arrange the density of the grid, the dimensional functions proximity and curvature are used. The mesh is refined in the place where the stress gradient is large. The quality of the grid has a greater impact on the calculation accuracy. Through the finite element-preprocessing software, the mesh

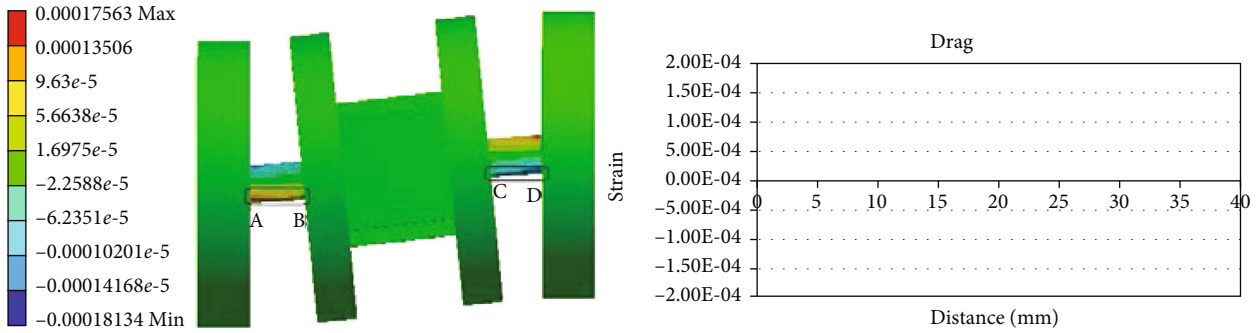

Figure 3: Strain cloud diagram and strain distribution of maximum resistance.

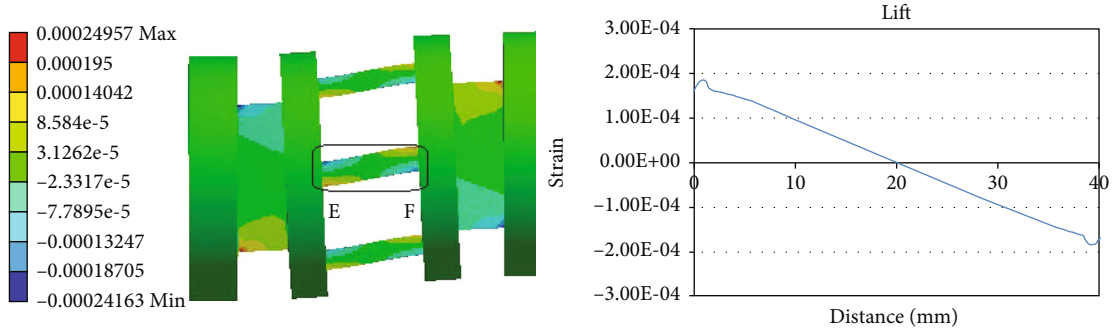

Figure 4: Strain cloud diagram and strain distribution of maximum lift.

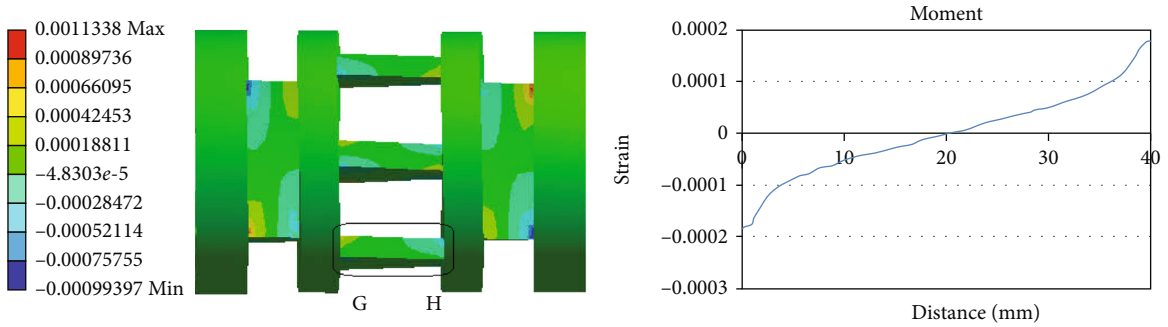

Figure 5: Strain cloud diagram and strain distribution of maximum pitching moment.

quality is checked and modified until the finite element model fully meets the high-precision requirements. In actual calculations, the calculation results of two different mesh densities are compared. If the calculation results are very different, you can continue to increase the grid until the calculation results are not much different and the grid size is appropriate.

2.3.3. Definition of Material Properties and Boundary Conditions. The material used in the design is with elastic modulus $E = 200GPa$ and yield strength $\sigma_S = 2020MPa$. According to the impact factor $n_c = 1.5$ and safety factor $n_a = 2$ selected in [8], the allowable stress can be obtained $[\sigma] = 673MPa$.

The following loads were applied for static calculations: (1) maximum resistance F_X, (2) maximum lift F_y, (3) maximum pitch moment M_Z, (4) maximum lateral force F_z, (5) maximum yaw moment M_y, (6) maximum roll moment M_x, and (7) maximum load of six components under test conditions.

2.3.4. Static Analysis and Results. Figures 3–5 are the strain cloud diagrams of strains under the action of maximum resistance F_X, maximum lift F_y, and maximum pitch moment M_Z, as well as the distribution diagrams along $\overrightarrow{DC}$, $\overrightarrow{BA}$, $\overrightarrow{EF}$, and $\overrightarrow{HG}$, respectively. It can be seen from the figure that the maximum strain is close to the endpoint of the elastic measuring element, the best choices for strain gauges, and the maximum strain values at each position are 175.63 $\mu\varepsilon$, 249.57 $\mu\varepsilon$, and 113.38 $\mu\varepsilon$, which cannot meet the sensitivity requirements.

From Figure 6, the maximum equivalent stress value of the model is $\sigma_r = 575MPa$, which is less than the allowable stress of the material.

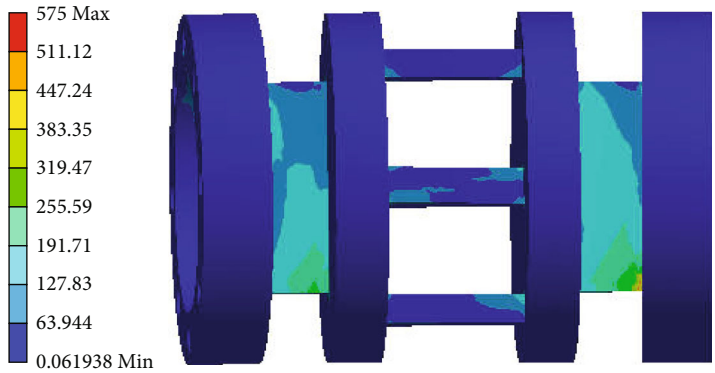

Figure 6: Strain cloud diagram of maximum load.

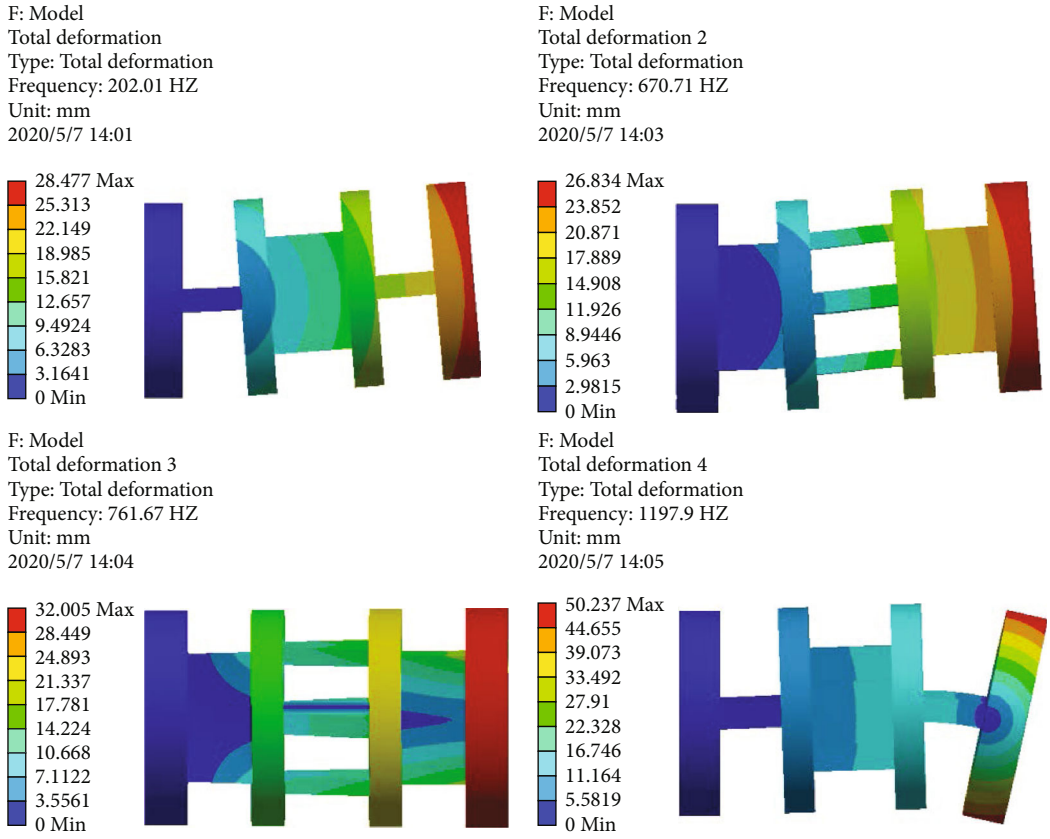

Figure 7: The shape of the first 4th-order splitting mode.

2.3.5. Modal Analysis and Results. In terms of resonance, all the modes whose natural frequency is in the range of the external load frequency should be maintained, and it must be calculated to be more than 10 times the operating frequency in this study. Therefore, the first 4 natural frequencies were selected to verify if they are in the resonance zone. The change of the first 4th-order mode shape of splitting is shown in Figure 7, and the natural frequency of each order is shown in Table 1.

2.4. Strain Gauge Position and Group Bridge. According to the strain cloud diagram and strain value distribution diagram [9–11], the installation position of the strain gauge is determined by comprehensively considering the paste technique and sensitivity requirements of the strain gauge. Wheatstone bridge was designed reasonably to achieve the largest possible output for the measured component [8] and the smallest possible output signal for other components, as well as achieve the electrical decomposition of force and torque. The final distribution of strain gauges and bridge formation are shown in Figures 8 and 9.

Table 1: Result of mode analysis.

Mode	1	2	3	4
Frequency	202.01	670.71	761.67	1197.9

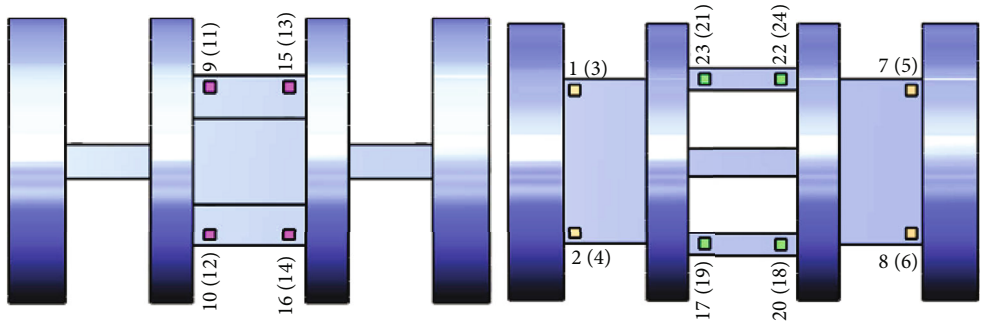

Figure 8: Layout of strain gauges.

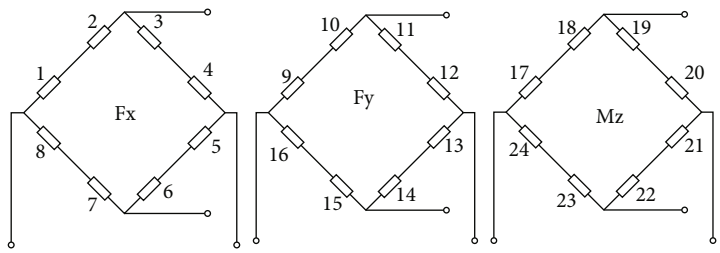

Figure 9: Wheatstone bridge diagram of each component.

3. Optimized Design of Sensor Split Structure

Parameter optimization is needed as the finite element analysis of the initial design of the sensor split proved that it cannot meet the sensitivity requirements. Appropriate design variables and output responses for experimental design were selected, and a sufficient number of finite element analysis sample points were generated to fit the approximate model; the optimization problem was defined, and the sensor parameters were optimized based on the NSGA-II multiobjective optimization algorithm.

3.1. Approximate Model and Verification. The RBF neural network approximate model is used in simulating the input-output relationship of the finite element model to solve the problem of huge time cost during calculation. The establishment of approximate models mainly is as follows:

(1) The input parameters were defined as x_i (x_i are the geometric parameters B1, B2, B3, H1, H2, H3, L1, L2, S1, S2, and P, $1 \le i \le 11, i \in N$) with a total of 11 input variables whose initial value and range of values are shown in Table 2

(2) The output parameters were defined as y_j, with the maximum equivalent stress $s_{\max}$ and the maximum deformation displacement value $d_{\max}$ under the maximum load of six components under test conditions, first-order natural frequency $freq1$; the average strain values ($\varepsilon_{xx1} \sim \varepsilon_{xx8}$, $\varepsilon_{xy1} \sim \varepsilon_{xy8}$, $\varepsilon_{xz1} \sim \varepsilon_{xz8}$, $\varepsilon_{xmx1} \sim \varepsilon_{xmx8}$, $\varepsilon_{xmy1} \sim \varepsilon_{xmy8}$, and $\varepsilon_{xmz1} \sim \varepsilon_{xmz8}$) of strain gauges 1-8 are under maximum resistance F_X, maximum lift F_y, maximum lateral force F_z, maximum roll moment M_x, maximum yaw moment M_y, and maximum pitch moment M_Z; average strain values ($\varepsilon_{yx1} \sim \varepsilon_{yx8}$, $\varepsilon_{yy1} \sim \varepsilon_{yy8}$, $\varepsilon_{yz1} \sim \varepsilon_{yz8}$, $\varepsilon_{ymx1} \sim \varepsilon_{ymx8}$, $\varepsilon_{ymy1} \sim \varepsilon_{ymy8}$, and $\varepsilon_{ymz1} \sim \varepsilon_{ymz8}$) of strain gauges 9-16 are under maximum resistance F_X, maximum lift F_y, maximum lateral force F_z, maximum roll moment M_x, maximum yaw moment M_y, and maximum pitch moment M_Z; average strain values ($\varepsilon_{mzx1} \sim \varepsilon_{mzx8}$, $\varepsilon_{mzy1} \sim \varepsilon_{mzy8}$, $\varepsilon_{mzz1} \sim \varepsilon_{mzz8}$, $\varepsilon_{mzmx1} \sim \varepsilon_{mzmx8}$, $\varepsilon_{mzmy1} \sim \varepsilon_{mzmy8}$, are $\varepsilon_{mzmz1} \sim \varepsilon_{mzmz8}$) of the serial number 17-24 strain gauges are under maximum resistance F_X, maximum lift F_y, maximum lateral force F_z, maximum roll moment M_x, maximum yaw moment M_y, and maximum pitch moment M_Z. A total of 148 output responses are set as output parameters

Table 2: Design parameters and value range.

Parameters	Lower bound	Value	Upper bound
$B1$	5	10	10
$B2$	4	8	8
$B3$	5	12	15
$H1$	25	40	45
$H2$	20	30	40
$H3$	50	60	80
$L1$	20	40	60
$L2$	10	30	40
$S1$	5	15	15
$S2$	12.5	20	22.5
P	30	34	50

Table 3: The error calculation results of an approximate model.

Index	R^2	Index	R^2	Index	R^2
$s_{\max}$	0.93	$\varepsilon_{xmy1} \sim \varepsilon_{xmy8}$	0.94~0.95	$\varepsilon_{mzx1} \sim \varepsilon_{zx8}$	0.97~0.98
$d_{\max}$	0.95	$\varepsilon_{xmz1} \sim \varepsilon_{xmz8}$	0.93~0.94	$\varepsilon_{mzy1} \sim \varepsilon_{mzy8}$	0.91~0.92
$freq1$	0.988	$\varepsilon_{yx1} \sim \varepsilon_{yx8}$	0.97~0.98	$\varepsilon_{mzz1} \sim \varepsilon_{mzz8}$	0.97~0.98
$mass$	1	$\varepsilon_{yy1} \sim \varepsilon_{yy8}$	0.97~0.98	$\varepsilon_{mzmx1} \sim \varepsilon_{mzmx8}$	0.97~0.98
$\varepsilon_{xx1} \sim \varepsilon_{xx8}$	0.94~0.95	$\varepsilon_{yz1} \sim \varepsilon_{yz8}$	0.96~0.97	$\varepsilon_{mzmy1} \sim \varepsilon_{mzmy8}$	0.94~0.95
$\varepsilon_{xy1} \sim \varepsilon_{xy8}$	0.97~0.98	$\varepsilon_{ymx1} \sim \varepsilon_{ymx8}$	0.94~0.95	$\varepsilon_{mzmz1} \sim \varepsilon_{mzmz8}$	0.97~0.98
$\varepsilon_{xz1} \sim \varepsilon_{xz8}$	0.94~0.95	$\varepsilon_{ymy1} \sim \varepsilon_{ymy8}$	0.94~0.96		
$\varepsilon_{xmx1} \sim \varepsilon_{xmx8}$	0.96~0.97	$\varepsilon_{ymz1} \sim \varepsilon_{ymz8}$	0.96~0.97		

(3) The optimal Latin hypercube test design method was used to obtain a sufficient number of sample points, and an approximate model of RBF neural network was established

(4) The cross-validation method was used to detect the accuracy of the approximate model. If the accuracy is insufficient, the approximate point is added to increase the approximate model to a sufficient accuracy

The credibility index R^2 was utilized as the evaluation index to detect the global and local approximation accuracy of the approximation model with a lower limit of 0.9. The closer the R^2 to 1, the more accurate.

From the approximate model error calculation results (shown in Table 3), it can be seen that the radial basis neural network approximate model exhibits good performance in fitting the sensor split finite element model.

3.2. Multiobjective Optimization. Taking the input parameters x_i of the above approximate model as the design variables, the average strain value $\varepsilon_1 \sim \varepsilon_{24}$ as the constraint, the minimizing of maximum equivalent stress $s_{\max}$, the maximum displacement value $d_{\max}$, the maximizing of first-order natural frequency $freq1$, and the minimizing of interference η_x, η_y, and η_{mz} of the components of F_X, F_y, and M_Z are the goal of optimizing. Then, the optimization problem was defined as below [12–15].

$$\begin{cases} \text{Minimize} : d_{\max}, Mass \\ \text{Minimize} : \eta_x, \eta_y, \eta_{Mz} \\ \text{Minimize} : s_{\text{Max}} \\ \text{Maximize} : freq1 \\ s.t\ 300\mu m \le \varepsilon_j \le 600\mu m, j \in [1, 24] \&\& j \in N \\ s_{\text{Max}} \le 673MPa \\ D.v. \quad x_i^{(L)} \le x_i \le x_i^{(U)} \\ \qquad i \in [1, 11] \&\& i \in N. \end{cases} \tag{1}$$

According to the principle of Wheatstone bridge, for resistance bridge, when $R \gg \triangle R$

$$U_o = \frac{U_i K}{8}(\varepsilon_1 + \varepsilon_2 - \varepsilon_3 - \varepsilon_4 + \varepsilon_5 + \varepsilon_6 - \varepsilon_7 - \varepsilon_8), \tag{2}$$

where U_o is the output voltage of the bridge, U_i is the supply voltage of the bridge, and K is the sensitivity coefficient of the strain gauge.

When the sensor is under the maximum load of each component, the output voltage of the resistance bridge is

$$\begin{aligned} U_o^{xx} &= \frac{U_i K}{8}(\varepsilon_{xx1} + \varepsilon_{xx2} - \varepsilon_{xx3} - \varepsilon_{xx4} + \varepsilon_{xx5} + \varepsilon_{xx6} - \varepsilon_{xx7} - \varepsilon_{xx8}), \\ U_o^{xy} &= \frac{U_i K}{8}(\varepsilon_{xy1} + \varepsilon_{xy2} - \varepsilon_{xy3} - \varepsilon_{xy4} + \varepsilon_{xy5} + \varepsilon_{xy6} - \varepsilon_{xy7} - \varepsilon_{xy8}), \\ U_o^{xz} &= \frac{U_i K}{8}(\varepsilon_{xz1} + \varepsilon_{xz2} - \varepsilon_{xz3} - \varepsilon_{xz4} + \varepsilon_{xz5} + \varepsilon_{xz6} - \varepsilon_{xz7} - \varepsilon_{xz8}), \\ U_o^{xmx} &= \frac{U_i K}{8}(\varepsilon_{xmx1} + \varepsilon_{xmx2} - \varepsilon_{xmx3} - \varepsilon_{xmx4} + \varepsilon_{xmx5} + \varepsilon_{xmx6} - \varepsilon_{xmx7} - \varepsilon_{xmx8}), \\ U_o^{xmy} &= \frac{U_i K}{8}(\varepsilon_{xmy1} + \varepsilon_{xmy2} - \varepsilon_{xmy3} - \varepsilon_{xmy4} + \varepsilon_{xmy5} + \varepsilon_{xmy6} - \varepsilon_{xmy7} - \varepsilon_{xmy8}), \\ U_o^{xmz} &= \frac{U_i K}{8}(\varepsilon_{xmz1} + \varepsilon_{xmz2} - \varepsilon_{xmz3} - \varepsilon_{xmz4} + \varepsilon_{xmz5} + \varepsilon_{xmz6} - \varepsilon_{xmz7} - \varepsilon_{xmz8}), \\ \eta_{xy} &= abs[(U_o^{xy})/U_o^{xx}], \\ \eta_{xz} &= abs[(U_o^{xz})/U_o^{xx}], \\ \eta_{xmx} &= abs[(U_o^{xmx})/U_o^{xx}], \\ \eta_{xmy} &= abs[(U_o^{xmy})/U_o^{xx}], \\ \eta_{xmz} &= abs[(U_o^{xmz})/U_o^{xx}], \\ \eta_x &= \eta_{xy} + \eta_{xz} + \eta_{xmx} + \eta_{xmy} + \eta_{xmz}. \end{aligned} \tag{3}$$

η_{yx}, η_{yz}, η_{ymx}, η_{ymy}, η_{ymz}, η_y, η_{mzx}, η_{mzy}, η_{mzz}, η_{mzmx}, η_{mzmy}, and η_{mz} can be obtained based on the same process.

Based on the established RBF neural network approximate model, the Pareto optimal solution (shown in Figure 10) was obtained by using the NSGA-II optimization algorithm after repeated experiments with a population size of 100, a cross-distribution index of 100, and a cross-probability of 0.9 in 6001 calculation steps.

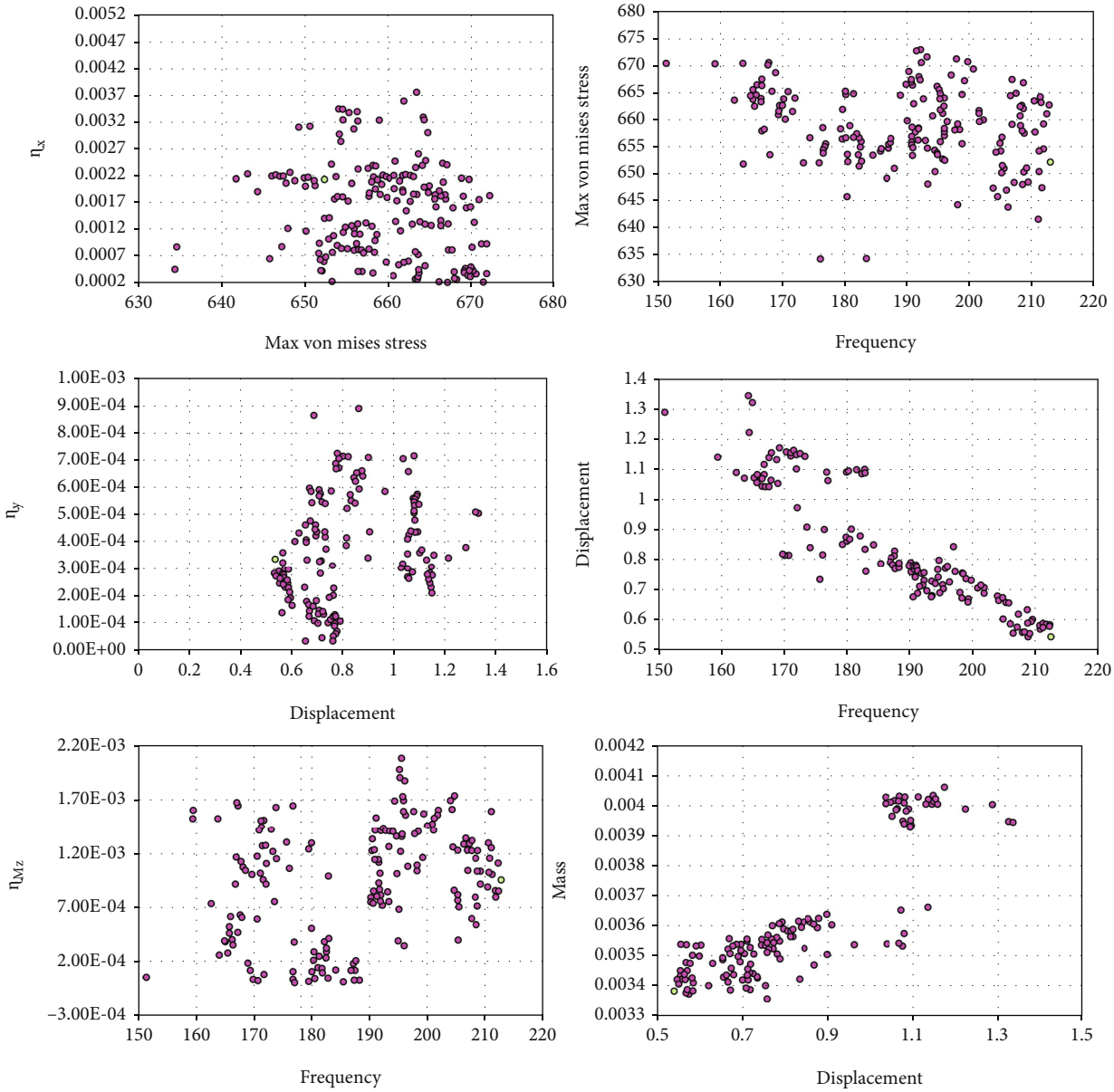

Figure 10: Pareto optimal solution.

After sorting the above solution sets, the 1896th is determined to be the optimal solution whose comparative analysis of the results is shown in Table 4.

In initial design, the initial interference η_x on the resistance F_X and the interference on the pitching moment M_Z are relatively large, reaching 4.26% and 5.12%, respectively; the strain values under the action of the maximum resistance F_X, the maximum lift F_y, and the maximum pitching moment M_Z are 81.6 $\mu\varepsilon$, 115.1 $\mu\varepsilon$, and 167.7 $\mu\varepsilon$, respectively, which cannot meet the technical requirements of the sensor split. After optimization, the strain values under the action of the maximum resistance F_X, the maximum lift F_y, and the maximum pitching moment M_Z are increased by 271%, 408%, and 227%, respectively, and the interference of the component is reduced by 95%, 94.4%, and 98.1%; the first-order natural frequency is increased by 5%, and the quality is reduced by 28.1%.

4. Robustness Analysis and Optimization

Some uncertain factors, such as the processing error of the sensor split and the assembly error between the sensor splits, are inevitable to encounter during the execution of the actual rotor blade wind tunnel test project. Without considering the influence of these uncertain factors in the deterministic optimization of the sensor split, the optimization result may present lower reliability or robustness and greater technical risks in practice [16, 17].

Therefore, it is necessary to further perform robust analysis and even optimization on the split parallel

Table 4: Optimization results.

Optimization goal	Initial value (mm)	Optimization value (mm)	Percent changed
s_{max}	575	652.33	13.45%
d_{max}	0.7413	0.5399	-27.17%
$freq1$ (Hz)	202.49	212.628	5%
Mass	0.0047	0.00338	28.1%
ε_x	81.6	302.6	271%
ε_y	115.1	585.19	408%
ε_{Mz}	167.7	548.62	22%
η_x	4.26%	0.214%	-95.0%
η_y	0.6125%	0.034%	-94.4%
η_{mz}	5.12%	0.098%	-98.1%

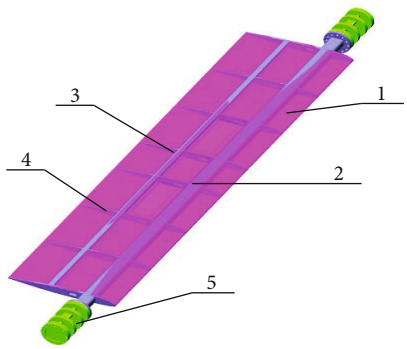

Figure 11: Three-dimensional diagram of the system. (a) Test model skin. (b) Test model front beam. (c) Test model rear beam. (d) Test model longitudinal beam. (e) Sensor split.

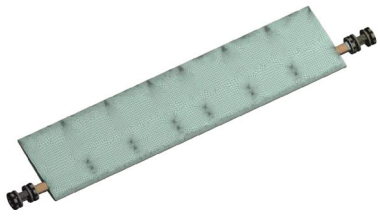

Figure 12: Grid division diagram.

Table 5: Mechanical parameters of T800 carbon fiber-reinforced composites.

Elastic modulus, GPa			Shear modulus, GPa			Poisson's ratio		
E_1	E_2	E_3	G_{12}	G_{13}	G_{23}	ν_{12}	ν_{13}	ν_{23}
195	8.58	8.58	4.6	4.6	2.9	0.33	0.33	0.48
Tensile strength, MPa			Compression strength, MPa			Shear strength, MPa		
X_T	Y_T	Z_T	X_C	Y_C	Z_C	S_{12}	S_{13}	S_{23}
3071	88	88	1747	271	271	143	143	143

Table 6: Material properties.

Material	Modulus (GPa)	Poisson's ratio	Density (kg m^{-3})
7075	72	0.33	2810

multicomponent strain sensor considering the interference of uncertain factors.

4.1. System Finite Element Model Analysis

4.1.1. Geometric Model. The scheme of analysis system is shown in Figure 11, consisting of main components such as front and rear beams, longitudinal beams, and skin with a total length of 1950 mm and a chord length of 300 mm. The binary model of OA309 airfoil is used in characterizing cross-section.

4.1.2. Pretreatment. Firstly, the model is simplified as below without affecting the calculation accuracy of the device.

(1) The fine process holes for nonconnections with little effect on the overall performance of the structure are ignored

(2) Small chamfers and rounded corners are removed

(3) The quality unit is used for the parts that do not participate in the analysis

(4) Quadrilateral shell elements are used to divide the grid after extracting the corresponding shell

Secondly, 4-node quadrilateral elements divided each component and were combined with the aforementioned sensor split grid to form an assembly (Figure 12) so as to ensure the accuracy and efficiency of the calculation, using the wind tunnel test model.

Finally, the material properties and boundary conditions are defined. The material of the front beam of the test model is 7075, and the rest of the test model is made of T800 carbon fiber-reinforced composite material. The material properties are shown in Tables 5 and 6. The applied loads and constraints are mainly composed of three aspects that are inertial load and aerodynamic load, the last one is one sensor split that is fixedly connected through the screw hole, and the other is applied with 6 degrees of freedom through the screw hole assembly error (Δx, Δy, Δz, $\Delta\alpha$, $\Delta\beta$, and $\Delta\gamma$).

4.1.3. Finite Element Static Analysis and Results. The von Mises stress is employed for strength evaluation according to the fourth strength theory. In Figure 13, the maximum equivalent stress value of the sensor $\sigma_r = 600.9$ MPa is smaller than the allowable stress of the material. Hence, the model is applicable.

4.1.4. Modal Analysis and Results. The first-order natural frequency of the system must be greater than 50 Hz. Figure 14 shows the first-order vibration mode of the system with natural frequency of 54.17 Hz.

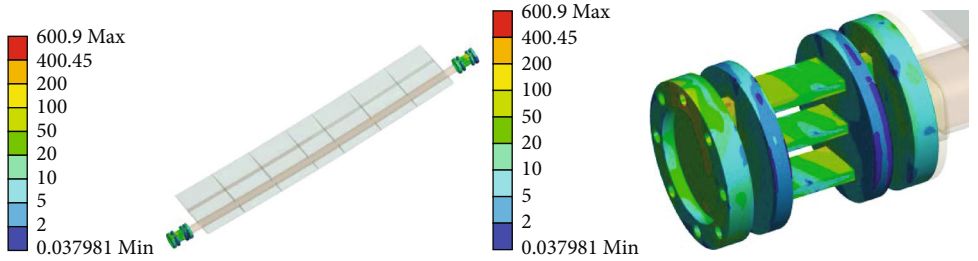

Figure 13: Stress contours of the model.

Figure 14: The first-order natural frequency of the system.

Table 7: Input parameters and value range.

Input parameters	Lower bound	Upper bound	Output parameters
$B1$	5	8	$s_{\max}$
$B2$	4	8	$freq1$
$B3$	5	15	$mass$
$H1$	25	45	
$H2$	20	40	
$H3$	50	80	
$L1$	20	60	
$L2$	10	40	
$S1$	5	15	
$S2$	12.5	22.5	
P	30	50	
Δx	0	0.3	
Δy	0	0.5	
Δz	0	0.2	
$\Delta\alpha$	0	0.15	
$\Delta\beta$	0	0.15	
$\Delta\gamma$	0	0.15	

Table 8: The error calculation results of an approximate model.

Index	R^2
$s_{\max}$	0.985
$freq1$	0.964
$mass$	0.992

4.2. System Approximate Model. The optimal Latin hypercube test design method is used to obtain a certain number of sample points, and a fourth-order polynomial response surface (RSM) approximate model is established. Input parameters and output parameters are shown in Table 7.

Credibility indicators (R^2) are taken as evaluation indicators. It can be seen from the calculation results of the approximate model error (Table 8) that the approximate model has good performance in fitting the system.

4.3. Robustness Analysis. The 6σ robustness analysis, the basis of the robustness optimization, is to evaluate the quality level of the deterministic optimization plan by disturbing the current design point, generating a set of sample points around its average value, and then estimating the quality level reliability failure rate and million defective rate of the output response index at a single design point through statistical analysis. At the same time, the average and standard deviation of each output response index are counted. The 6σ robustness analysis assumes that the product performance distribution is a normal distribution, and the distance between the mean value of the performance index and the quality constraint is $\pm 6\sigma$.

$$\begin{cases} \text{Minimize} : \mu(Mass) + 6\sigma \\ \text{Minimize} : \mu\left(\eta_x, \eta_y, \eta_{Mz}\right) + 6\sigma \\ \\ \quad \mu\left(\eta_x, \eta_y, \eta_{Mz}\right) + 6\sigma \le 0.01 \\ s.t \quad \mu\left(\varepsilon_j\right) - 6\sigma \ge 300\mu\varepsilon \\ \quad \mu\left(\varepsilon_j\right) + 6\sigma \le 600\mu\varepsilon \\ \mu(s_{Max}) + 6\sigma \le 673MPa \\ \mu(freq1) - 6\sigma \le 50Hz \\ j \in [1, 24] \&\& j \in N \\ j \in [1, 24] \&\& j \in N \\ \\ D.v. \quad x_i^{(L)} \le x_i \le x_i^{(U)} \\ \quad i \in [1, 17] \&\& i \in N. \end{cases} \tag{4}$$

Table 9: Random noise variables and values of probability density function (distribution type, average, and coefficient of variation).

Input parameter	Distribution type	Average	Coefficient of variation
$B1$	Normal	5.76	1%
$B2$	Normal	5.29	1%
$B3$	Normal	7.59	1%
$H1$	Normal	33.56	0.1%
$H2$	Normal	29.38	0.1%
$H3$	Normal	65.18	0.1%
$L1$	Normal	43.33	0.1%
$L2$	Normal	12.62	0.5%
$S1$	Normal	13.59	0.5%
$S2$	Normal	15.94	0.5%
P	Normal	40.18	0.1%

Table 10: Random noise variables and values of probability density function (distribution type and range).

Input parameter	Distribution type	Range
Δx	Uniform	[0,0.3]
Δy	Uniform	[0,0.5]
Δz	Uniform	[0,0.2]
$\Delta\alpha$	Uniform	[0, 0.1°]
$\Delta\beta$	Uniform	[0, 0.1°]
$\Delta\gamma$	Uniform	[0, 0.1°]

Based on the results of the deterministic optimization of the above sensor splits and the assembly errors between the splits, the sensor split approximate model and the system approximate model are combined. The Monte Carlo sampling is used to evaluate the quality level of the deterministic optimization plan, and 11 design variables and assembly error variables (the relative displacement and angular error between the two sensor splits: three displacement errors, Δx, Δy, and Δz, and three angular errors, $\Delta\alpha$, $\Delta\beta$, and $\Delta\gamma$) are selected as the noise factor (Tables 9 and 10). Based on the combined approximation model, the sample points were collected by descriptive sampling method with 100 sampling times to obtain the quality level of the deterministic optimization plan. As shown in Table 11, the quality levels of maximum equivalent stress $s_{\max}$, first-order natural frequency $freq1$, and the strain ε_x and ε_{Mz}, under the action of the maximum resistance F_X, and the maximum pitching moment M_Z are 1.414 σ, 1.636 σ, and 1.31 σ, which cannot reach the level of robustness quality, and robustness optimization is required. The robustness optimization of the split-parallel multicomponent strain-type force sensor is still based on the approximation model established above. The descriptive sampling method is used to collect sample points. The value ranges of design variables and noise factors are shown in Tables 9, 10,

Table 11: Comparison of robustness before and after optimization.

Input parameter	Deterministic optimization value		Robust optimization value	
	Solution	6σ analysis	Solution	Quality level
$B1$	5.76	8	5.97	8
$B2$	5.29	8	5.86	8
$B3$	7.59	8	7.35	8
$H1$	33.56	8	33.78	8
$H2$	29.38	8	34.30	8
$H3$	65.18	8	64.78	8
$L1$	43.33	8	41.60	8
$L2$	12.62	8	15.04	8
$S1$	13.59	8	12.67	8
$S2$	15.94	8	14.85	8
P	40.18	8	35.49	8
Δx	0	8	0	8
Δy	0	8	0	8
Δz	0	8	0	8
$\Delta\alpha$	0	8	0	8
$\Delta\beta$	0	8	0	8
$\Delta\gamma$	0	8	0	8
ε_x	302.65	1.516	314.54	8
ε_y	585.19	8	443.08	8
ε_{Mz}	548.62	1.31	421.79	8
η_x	0.214%	8	0.093%	8
η_y	0.034%	8	0.0439%	8
η_{mz}	0.098%	8	0.008%	8
$s_{\max}$	600.9	1.414	419.3035	8
$freq1$	54.713	1.636	53.27	8
$mass$	0.00338		0.00349	

Table 12: Design variables and value ranges.

Input parameter	Lower bound	Upper bound
$B1$	5	8
$B2$	4	8
$B3$	5	15
$H1$	25	45
$H2$	20	40
$H3$	50	80
$L1$	20	60
$L2$	10	40
$S1$	5	15
$S2$	12.5	22.5
P	30	50

Table 13: Comparison of results before and after two optimizations.

Optimization goal	Initial value	Optimization value	Percent changed
Mass	0.0047	0.00349	-25.74%
ε_x	81.6	314.54	285.46%
ε_y	115.1	443.08	284.95%
ε_{Mz}	167.7	421.79	151.5%
η_x	4.26%	0.093%	-97.82%
η_y	0.6125%	0.0439%	-92.83%
η_{mz}	5.12%	0.008%	-99.8%

and 12. Algorithm NSGA-II is used for robust optimization. Through robust multiobjective optimization, the sensor output parameters can reach a quality level above 6 sigma (Table 11). By comparing the parameters before and after the robustness optimization (Table 13), it is found that the sensitivity of the three components increases by 14.73%, 21.2%, and 29.3%, respectively, when the quality of the sensor increases slightly and the amount of interference changes little.

5. Conclusions

(1) A split parallel multicomponent strain sensor structure layout is proposed to satisfy the special requirements for the measurement of aerodynamic sensors by the helicopter rotor airfoil wind tunnel test

(2) A finite element analysis model is established with the sensor split as the object to analyze separately its strain under the action of resistance, lift, and pitch moment cloud map and to determine the location of strain gauges and the way of group bridges

(3) The RBF neural network approximate model and NSGA-II multiobjective optimization algorithm are utilized to deterministically optimize the sensor split performance and obtain excellent monomer performance. Satisfying the strength and rigidity, the strain values under the action of the maximum resistance F_X, the maximum lift F_y, and the maximum pitching moment M_Z of the sensor split structure are increased by 271%, 408%, and 227%, respectively, and the interference of the component is reduced by 95%, 94.4%, and 98.1%; the first-order natural frequency is increased by 5%, and the quality is reduced by 28.1%

(4) Based on the above deterministic optimization, the split manufacturing error and the assembly error between the splits are introduced, and the sensor and rotor airfoil test model-integrated finite element system model and RSM approximate model are successively established by using the Monte Carlo sampling method to check the quality level of the system and 6σ robustness optimization to improve the robustness of the sensor and reduce the sensitivity of the response to assembly and manufacturing errors

(5) Through 6σ robustness analysis based on deterministic optimization, the robustness of the sensor was improved, and the sensitivity of the response to assembly and manufacturing errors were reduces

(6) After these two optimizations, satisfying the strength and rigidity and considering the random noise effect of the split manufacturing error and the assembly error between the splits, the strain value of the maximum resistance F_X, the maximum lift F_y, and the maximum pitching moment M_Z of the sensor were increased by 285.46%, 284.95%, and 151.5%, respectively, the interference to the three components was reduced by 97.82%, 92.83%, and 99.8%, respectively, and the quality was reduced by 25.74%. At the same time, the sensor quality level reached 6σ

Data Availability

No data were used to support this study.

Conflicts of Interest

The authors declare no conflict of interest.

References

[1] A. R. Tavakolpour-Saleh, A. R. Setoodeh, and M. Gholamzadeh, "A novel multi-component strain-gauge external balance for wind tunnel tests: simulation and experiment," *Sensors & Actuators A Physical*, vol. 247, pp. 172–186, 2016.

[2] L. Zhao, Y. Yan, X. Yan, and L. Zhao, "Structural parameters optimization of elastic cell in a near-bit drilling engineering parameters measurement sub," *Sensors*, vol. 19, no. 15, 2019.

[3] R. P. Ubeda, S. C. Gutiérrez Rubert, R. Z. Stanisic, and Á. P. Ivars, "Design and manufacturing of an ultra-low-cost custom torque sensor for robotics," *Sensors*, vol. 18, no. 6, 2018.

[4] V. Grosu, S. Grosu, B. Vanderborght, D. Lefeber, and C. Rodriguez-Guerrero, "Multi-axis force sensor for human-robot interaction sensing in a rehabilitation robotic device," *Sensors*, vol. 17, no. 6, p. 1294, 2017.

[5] X.-L. Zhang, T. Wu, Y. Shao, and J. Song, "Structure optimization of wheel force transducer based on natural frequency and comprehensive sensitivity," *Journal of Sound and Vibration*, vol. 30, no. 4, pp. 973–981, 2017.

[6] D. He, *Wind tunnel balance*, National Defense Industry Press, 1999.

[7] R. A. B. Almeida, D. C. Vaz, A. P. V. Urgueira, and A. R. Janeiro Borges, "Using ring strain sensors to measure dynamic forces in wind-tunnel testing," *Sensors and Actuators A: Physical*, vol. 185, pp. 44–52, 2012.

[8] Y. Li, Y. Zhao, J. Fei et al., "Design and development of a three-component force sensor for milling process monitoring," *Sensors*, vol. 17, no. 5, 2017.

[9] Y. Sun, Y. Liu, T. Zou, M. Jin, and H. Liu, "Design and optimization of a novel six-axis force/torque sensor for space robot," *Measurement*, vol. 65, pp. 135–148, 2015.

[10] S. Hu, H. Wang, Y. Wang, and Z. Liu, "Design of a novel six-axis wrist force sensor," *Sensors*, vol. 18, no. 9, p. 3120, 2018.

[11] J. Ma and A. Song, "Fast estimation of strains for cross-beams six-axis force/torque sensors by mechanical modeling," *Sensors*, vol. 13, no. 5, pp. 6669–6686, 2013.

[12] A. Witoniowski and A. Bar, "Parametrical excitement vibration in tandem mills–mathematical model and its analysis," *Journal of Materials Processing Technology*, vol. 134, no. 2, pp. 214–224, 2003.

[13] A. Batish, A. Bhattacharya, M. Kaur et al., "Hard turning: parametric optimization using genetic algorithm for rough/finish machining and study of surface morphology," *Journal of Mechanical Science & Technology*, vol. 28, no. 5, pp. 1629–1640, 2014.

[14] G. Huang, D. Zhang, S. Guo, and H. Qu, "Design and optimization of a novel three-dimensional force sensor with parallel structure," *Sensors*, vol. 18, no. 8, p. 2416, 2018.

[15] D. D. Nguyen and C. H. Kuo, "Design and optimization of a joint torque sensor for lightweight robots," *IEEE Sensors Journal*, vol. 21, no. 8, pp. 9788–9797, 2021.

[16] C. L. Fu, Y. C. Bai, C. Lin, and W. W. Wang, "Design optimization of a newly developed aluminum-steel multi-material electric bus body structure," *Structural & Multidisciplinary Optimization*, vol. 60, no. 5, pp. 2177–2187, 2019.

[17] X. Hu, R. Bao, W. Chen, and H. Wang, "Robust optimal design of strain-gauge-based force sensors using moving morphable components method: enhanced sensitivity and reduced cross-interference," *Structural and Multidisciplinary Optimization*, vol. 64, no. 3, pp. 1439–1455, 2021.